Snowflake Divertor Experiments in the DIII-D, NSTX, and NSTX-U Tokamaks Aimed at the Development of the Divertor Power Exhaust Solution

V. A. Soukhanovskii, S. L. Allen, M. E. Fenstermacher, C. J. Lasnier, M. A. Makowski, A. G. McLean, E. T. Meier, W. H. Meyer, T. D. Rognlien, D. D. Ryutov, F. Scotti, E. Kolemen, R. E. Bell, A. Diallo, S. Gerhardt, R. Kaita, S. Kaye, B. P. LeBlanc, R. Maingi, J. E. Menard, M. Podesta, A. L. Roquemore, R. J. Groebner, A. W. Hyatt, A. W. Leonard, T. H. Osborne, T. W. Petrie, J.-W. Ahn, R. Raman, and J. G. Watkins

***Abstract*— Experimental results from the National Spherical Torus Experiment (NSTX), a medium-size spherical tokamak with a compact divertor, and DIII-D, a large conventional aspect ratio tokamak, demonstrate that the snowflake (SF) divertor configuration may provide a promising solution for mitigating divertor heat loads and target plate erosion compatible with core H-mode confinement in the future fusion devices, where the standard radiative divertor solution may be inadequate. In NSTX, where the initial high-power SF experiment was performed, the SF divertor was compatible with H-mode confinement, and led to the destabilization of large Edge Localized Modes (ELMs). However, a stable partial detachment of the outer strike point was also achieved where inter-ELM peak heat flux was reduced by factors 3–5, and peak ELM heat flux was reduced by up to 80% (see standard divertor). The DIII-D studies show the SF divertor enables significant power spreading in attached and radiative divertor conditions. Results include: compatibility with the core and pedestal, peak inter-ELM divertor heat flux reduction due to geometry at lower n_e, and ELM energy and divertor peak heat flux reduction, especially prominent in radiative D_2-seeded SF divertor, and nearly complete power detachment and broader radiated power distribution in the radiative D_2-seeded SF divertor at $P_{SOL} = 3 - 4$ MW. A variety of SF configurations can be supported by the divertor coil set in NSTX Upgrade. Edge transport modeling with the multifluid edge transport code UEDGE shows that the radiative SF divertor can successfully reduce peak divertor heat flux for the projected $P_{SOL} \simeq 9$ MW case. The radiative SF divertor with carbon impurity provides a wider n_e operating window, 50% less argon is needed in the impurity-seeded SF configuration to achieve similar q_{peak} reduction factors (see standard divertor).**

***Index Terms*— Divertors, plasma materials interactions, tokamaks.**

I. Introduction

AN AXISYMMETRIC poloidal magnetic X-point divertor is the present vision for the tokamak plasma-material interface. The divertor enables access to high core and pedestal plasma performance regimes while keeping target plate heat loads and erosion within the operating limits of plasma-facing component cooling technology and target materials. The proposed ITER divertor is based on standard X-point geometry designs tested in large tokamak experiments: vertical targets with partial radiative detachment of the strike points are used. However, the standard radiative divertor approach is likely to be insufficient for next step advanced tokamak and spherical tokamak (ST) devices such as the proposed fusion nuclear science facilities or the DEMO reactor. Magnetic divertor configuration development and optimization aimed at particle and power exhaust control has been an active area of fusion research since the 1970s [1]. Many advanced divertor concepts (with respect to the standard divertor) rely on modifications to parallel and perpendicular transport, dissipative loss channels, and increased plasma-wetted area via modification of the magnetic configuration.

A snowflake (SF) divertor configuration [2] is a promising tokamak power exhaust concept that has received experimental support from Tokamak à configuration variable [3], National Spherical Torus Experiment (NSTX) [4], DIII-D [5], and EAST tokamaks [6]. The SF magnetic configuration uses a

Manuscript received July 31, 2015; revised July 12, 2016; accepted July 29, 2016. Date of publication November 16, 2016; date of current version December 16, 2016. This work was supported by the U.S. Department of Energy under Contract DE-AC52-07NA27344, Contract DE-AC02-09CH11466, Contract DE-FC02-04ER54698, Contract DE-FG02-07ER54917, and Contract DE-AC04-94AL85000.

V. A. Soukhanovskii, S. L. Allen, M. E. Fenstermacher, C. J. Lasnier, M. A. Makowski, A. G. McLean, E. T. Meier, W. H. Meyer, T. D. Rognlien, D. D. Ryutov, and F. Scotti are with the Lawrence Livermore National Laboratory, Livermore, CA 94550 USA.

E. Kolemen, R. E. Bell, A. Diallo, S. Gerhardt, R. Kaita, S. Kaye, B. P. LeBlanc, R. Maingi, J. E. Menard, M. Podesta, and A. L. Roquemore are with the Princeton Plasma Physics Laboratory, Princeton, NJ 08543-0451 USA.

R. J. Groebner, A. W. Hyatt, A. W. Leonard, T. H. Osborne, and T. W. Petrie are with the General Atomics, San Diego, CA 92186-5608 USA.

J.-W. Ahn is with the Oak Ridge National Laboratory, Oak Ridge, TN 37831 USA.

R. Raman is with the University of Washington, Seattle, WA 98195 USA.

J. G. Watkins is with the Sandia National Laboratories, Livermore, CA 94551-0969 USA.

Color versions of one or more of the figures in this paper are available online at http://ieeexplore.ieee.org.

Digital Object Identifier 10.1109/TPS.2016.2625325

TABLE I

PLASMA AND ENGINEERING PARAMETERS IN THE NSTX AND DIII-D SF DIVERTOR EXPERIMENTS, AND THE PLANNED ONES FOR NSTX-U. P_{NBI} IS THE NEUTRAL BEAM INJECTION INPUT POWER. I_p IS THE PLASMA CURRENT. λ_q IS THE SOL POWER WIDTH. fEXP IS THE POLOIDAL MAGNETIC FLUX EXPANSION AT THE DIVERTOR STRIKE POINT. $L_{\parallel}$ IS THE MAGNETIC FIELD LINE LENGTH (CONNECTION LENGTH) FROM MIDPLANE TO DIVERTOR TARGET ADJACENT TO SEPARATRIX (AT 0.1 mm AS MAPPED TO MIDPLANE). D IS THE INTERNULL DISTANCE FROM THE THEORETICAL SF CRITERION DISCUSSED IN TEXT

	Minor radius a (m)	P_{NBI} (MW)	I_p (MA)	λ_q (mm)	f_{exp} Standard / SF	$L_{\parallel}$ (m) Standard / SF	D (m)
NSTX	0.58	4	0.9	5-6	10-20 / 30-80	10-12 / 15-60	0.125
DIII-D	0.60	5	1.2	2.5-3	10 / 30-40	50 / 50-150	0.1
NSTX-U	0.62	≤ 12	≤ 2	~ 3	10-20 / 40	7-15 / 20-30	0.11

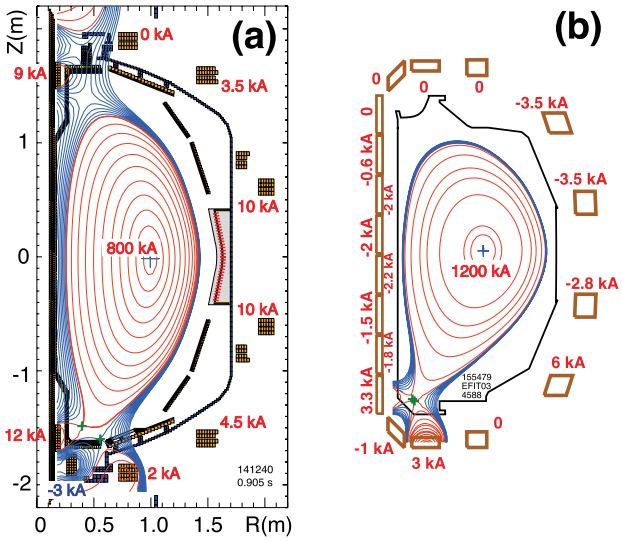

Fig. 1. Experimental equilibria with (a) SF-minus divertor configurations obtained in NSTX and (b) near-exact SF divertor configurations obtained in DIII-D tokamaks. Plasma currents and poloidal field coil currents are shown.

second-order null point created by superimposing two first-order poloidal field nulls, leading to the SF-like separatrix branches in the region of the exact second-order null, and a broader low B_p region, due to a quadratic B_p dependence on the distance from the null (versus linear B_p dependence in the standard divertor). These magnetic properties have a strong impact on divertor transport and heat deposition on plasma-facing components, owing to the increased divertor plasma-wetted area, increased X-point-to-target connection length and divertor volume, and additional divertor legs (strike points) where heat and particles can flow [2], [7], [8]. In this paper, we summarize key SF findings in high divertor power-density experiments in the NSTX and DIII-D tokamaks, planning new SF experiments in NSTX Upgrade, and discuss the SF concept development for future devices.

II. MAGNETIC EQUILIBRIA AND CONTROL

SF divertor configurations have been developed and demonstrated on the medium-size ST NSTX and the large conventional aspect ratio tokamak DIII-D. Both tokamaks have open divertors with graphite plasma-facing components and divertor heat fluxes of several MW/m^2. Both tokamaks have a similar poloidal field coil layout. Three magnetic coils are available for the SF configuration in the divertor region (Fig. 1). The exact second-order null configuration is topologically unstable [2], and therefore, in experiments, the following variants are realized in steady state [9], [10]: 1) the SF-plus, where the secondary null is at a small finite distance on the private flux region side of the standard divertor X-point; 2) the SF-minus, where the secondary null is in the common flux scrape-off layer (SOL) region, on the low filed side, or on the high field side; and 3) the near exact SF, where the distance between the nulls is approaching zero, while the configuration is fluctuating between SF-plus, SF-minus, and exact SF. The plasma control systems in both tokamaks are similar. Preprogrammed coil currents and strike point position control by the plasma control system (as in [11]) were used for SF-minus configurations. A real-time null-tracking algorithm was used for control of the near exact SF and SF-plus [12]. The SF configurations were sustained for periods comparable with plasma discharge duration, exceeding many energy confinement times: up to 0.5 s in NSTX, and for 2–3 s in DIII-D.

Under certain conditions, the derivative SF configurations, the SF-plus and SF-minus, have similar properties to those of the exact second-order null SF configuration. Two criteria have been developed theoretically for the separation of the poloidal field nulls to describe the situations when the SF-plus and the SF-minus are similar to the exact SF in: 1) geometry properties and 2) enhanced transport, leading to the power sharing between four strike points [7]. It is noted that the geometry and transport properties in the SF-plus and the SF-minus may be affected even when the internull distances are larger than those suggested by the criteria. The criteria provide guiding estimates as to when the second null affects the geometric and transport properties most significantly. The SF-plus and SF-minus geometry parameters, e.g., the poloidal magnetic flux expansion, the magnetic connection length, and the divertor specific volume are increased with respect to the standard divertor similar to the exact SF configuration when the distance D between nulls satisfies $D \leq a\ (\lambda_q/a)^{1/3}$ [where a is the minor radius and λ_q is the SOL power width (projected to midplane)]. The criterion for the enhanced transport in the SF-plus and SF-minus is $D \leq D^* \sim a\ (a\beta_{\mathrm{pm}}/R)^{1/3}$, where D^* is the radius of the high-convection zone in the null region, expressed as a function of a, R and the midplane poloidal β_{pm}. The appropriate parameters realized in the NSTX and DIII-D experiments are summarized in Table I. The internull distance D obtained in the experiments is within 50% of the estimated.

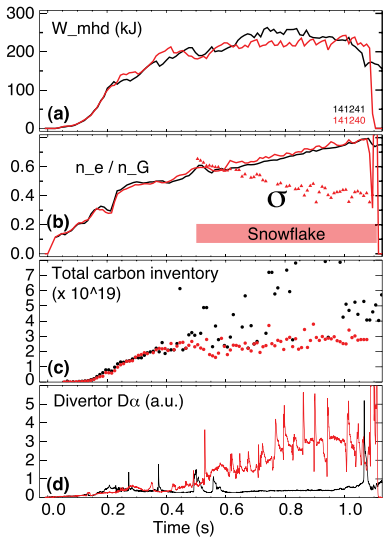

Fig. 2. Time traces of the H-mode discharges with the standard divertor (black) and SF (red) in NSTX. (a) Plasma stored energy W_{MHD}. (b) n_e/n_G and σ. (c) Total carbon inventory N_C. (d) Lower divertor D_α intensity.

III. Snowflake Divertor Experiments in NSTX

The SF divertor experiments were performed using highly shaped, lower single null biased ($dr_{\mathrm{sep}} \simeq 6-7$ mm, the midplane radial distance between separatrices corresponding to the lower and upper main X-points) $I_p = 0.8$ MA H-mode discharges with 4-MW NBI heating at $B_t = 0.45$ T and the ion ∇B direction toward the lower divertor. The SOL power (estimated from the core power balance) was $P_{\mathrm{SOL}} \simeq 3$ MW. Lithium coatings were used for wall conditioning and fuel inventory control in the amount of 80–100 mg per discharge. The core plasmas with SF configurations had similar shaping parameters with respect to those achieved with the standard divertor: the plasma volume ($V \simeq 12$ m^3) and elongation ($\kappa \simeq 2.2$–2.4) were unchanged, whereas the bottom triangularity was slightly reduced ($\delta \sim 0.65$–0.8).

The SF configuration was compatible with high confinement plasma operation, with no degradation in H-mode core performance [4], [11]. Shown in Fig. 2 are the time traces of two discharges with the standard and the SF configurations. The SF configuration was realized at $n_e/n_G \simeq 0.6$–0.8. Core plasma parameters ($\bar{n}_e$, central $T_e \leq 1$ keV, and $\beta_N \leq 4.5$) were similar in the two discharges. Similar high-performance metrics of these discharges, e.g., $\tau_E \simeq 50$–60 ms, $W_{\mathrm{MHD}} \simeq 200$–$250$ kJ, and the confinement factor H98$(y, 2) \simeq 1$, confirmed minimal, if any, impact of the SF phase on confinement. In these high-triangularity plasmas, the L-H transition power threshold was fairly low (about 1 MW), and therefore, no H-mode threshold studies were performed. The transition to the SF configuration in NSTX led to a clear and reproducible destabilization of ELMs. As the normalized internull distance $\sigma = D/a$ (where D is the internull distance and $a = 0.60$–0.62 m is the minor radius) became less than 0.5, large ELMs were evident on the lower divertor D_α time traces [Fig. 2(b) and (d)]. These large ELMs were classified as Type I, with somewhat irregular frequency of $f = 12$–35 Hz and $\Delta W_{\mathrm{MHD}}/W_{\mathrm{MHD}} \leq 15\%$.

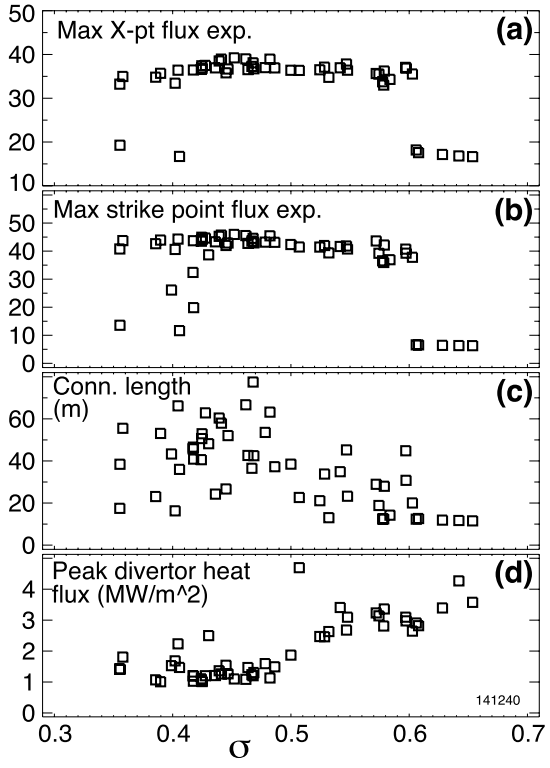

Fig. 3. Divertor geometry parameters and between-ELM peak heat flux as the functions of σ in NSTX: maximum $f$exp in (a) X-point and (b) outer strike point regions. (c) Connection length $L_\parallel$. (d) Peak heat flux.

In the standard divertor H-mode discharge, lithium coatings on lower divertor Plasma Facing components (PFCs) reduced recycling and led to modified edge plasma pressure and current profiles and low-n peeling-ballooning mode stabilization [13], [14], as the pedestal stability operating point was close to the peeling boundary. Depending on the lithium conditioning and other operational factors, ELMs were completely or partially suppressed in standard divertor H-mode discharges. Understanding of the SF pedestal stability in NSTX is complicated by this and other factors, e.g., the uncertainties in the electron pressure gradient and edge toroidal current density, plasma shaping changes (e.g., bottom triangularity), and the radiative detachment that accompanied the SF transition. In general, in the SF phase, the pedestal T_e was slightly reduced, while the pedestal n_e was also reduced due to reduced carbon density. The SF divertor phase had a strong effect on plasma impurity content [Fig. 2(c)]: the total carbon inventory N_c was reduced by 50%–70%. The observed reduction was attributed to the particle expulsion effect from the ELMs in the SF phase [11].

The SF-minus geometry had a strong impact on divertor properties in NSTX. The SF-minus formation always led to a stable partial detachment of the outer strike point, otherwise inaccessible in the standard divertor at $P_{\mathrm{SOL}} = 3$ MW at $n_e/n_G = 0.6$–0.8 [15], [16]. A significant inter-ELM reduction of divertor peak heat flux was measured [4], [11]. The heat flux reduction was interpreted as driven by both the geometric changes ($L_\parallel$ and A_w) and the increased radiative and momentum losses. Shown in Fig. 3 are divertor geometry

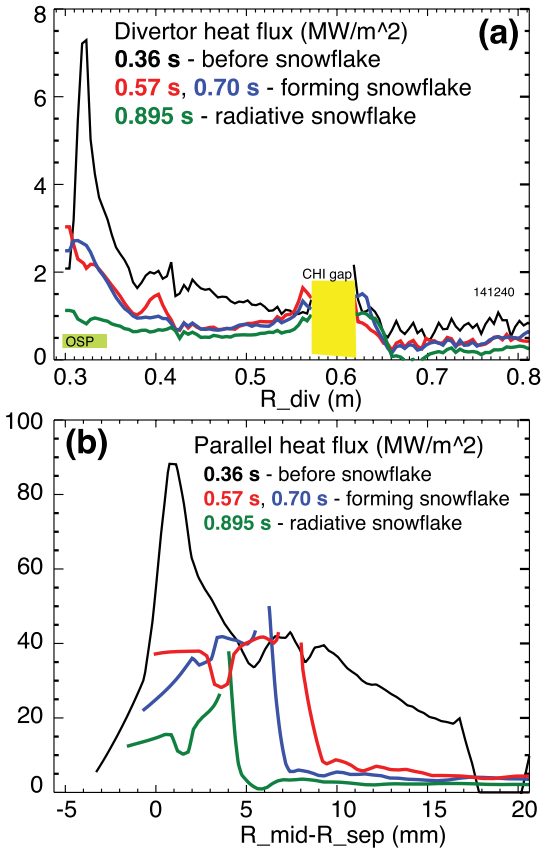

Fig. 4. (a) Divertor heat flux profiles before, during, and after SF-minus formation in NSTX. (b) Parallel heat flux profile projected to the midplane.

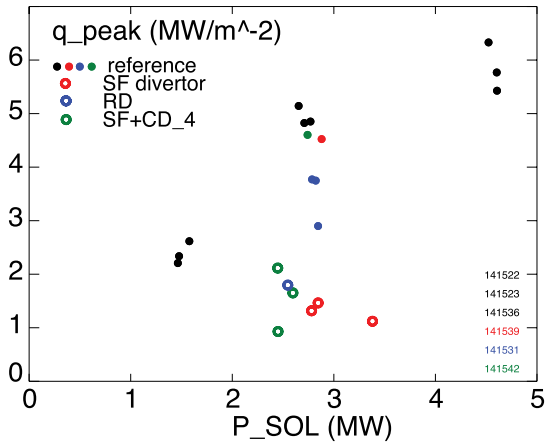

Fig. 5. Peak divertor heat flux q_{peak} as a function of SOL power P_{SOL} for the standard divertor discharges (filled circles) and the RD and SF discharges (open circles) in NSTX.

factors and peak heat flux between ELMs as the functions of the σ parameter. The X-point flux expansion is defined in a similar way to the strike point flux expansion: $f\exp = (B_p/R)_{\text{MP}}((B_p/R)\text{div})^{-1}$, where B_p is the poloidal magnetic field, and Rdiv is the major radius, taken either at the strike point or the X-point vicinity. The connection length is defined as magnetic field line length between midplane and divertor target adjacent to the separatrix. Fairly clear trends can be seen albeit some data scatter. Note that the σ parameter was large ($\sigma \geq 0.6$, if meaningful) for the standard divertor, and the data for $\sigma \geq 0.65$ are not plotted. During the transition from the standard to SF geometry ($\sigma = 0.55 - 0.65$), divertor q_{peak} decreased concomitantly with increasing $f\exp$ and $L_{\parallel}$. At $\sigma \leq 0.55$, a partial strike point detachment was observed, apparently driven by further increases in the SOL collisionality and volumetric losses from increased $L_{\parallel}$ and divertor volume. Fig. 4 shows the divertor heat flux profiles and the inferred parallel heat flux profiles mapped to the midplane at various times. During the SF formation period that lasted for 100–200 ms, divertor power decreased from 1.8–2 MW to about 1.2 MW, and the peak heat flux was reduced from 4–7 MW/m^2 to 2–3 MW/m^2 between ELMs. After the onset of detachment ($t \simeq 0.700$ s), q_{peak} further decreased to 0.5–1 MW/m^2, while the total power received by the outer divertor decreased to below 1 MW. The parallel heat flux profiles showed flattening and subsequent reduction across λ_q. The peaking of $q_{\parallel}$ at about 5–7 mm may be due to both the secondary separatrix heat flux and the edge tile CHI gap effect.

We note, however, that the parallel heat fluxes are also likely to be affected by enhanced radiation and cannot be interpreted as due to radial transport only. A detailed comparison of divertor impurity radiation and recombination profiles in the SF-minus was presented elsewhere [11]. In spite of the formation of the highly radiating detached region in the SF divertor, high core confinement was maintained.

The peak heat flux reduction in the SF configuration (without D_2 seeding) was similar to that measured in the radiative divertor experiments in the standard divertor geometry with D_2 or CD_4 seeding at similar $P_{\text{SOL}} \sim 3$ MW. These results are summarized in Fig. 5. Experiments were also performed with additional CD_4 or D_2 seeding into the SF phase using a divertor gas injector. In the CD_4-seeded SF divertor, the divertor C III and C IV brightness profiles showed (see standard radiative divertor) increased radiation, both in the intensity, and in the spatial extent. Excellent divertor gas screening from the core, increased divertor radiation, and stable MARFE-free operation (unaffected confinement) were demonstrated [17].

The SF-minus configuration had a strong impact on ELM heat fluxes in NSTX (Fig. 6). Peak heat fluxes from Type I ELMs were significantly reduced, from about 5–20 MW/m^2 in the standard divertor phase of the discharge, to 6–8 MW/m^2 during the SF formation phase and eventually below 2 MW/m^2 in the radiative SF phase. Peak target temperatures, measured by infrared thermography at peak ELM times, reached 1000 °C–1200 °C in the standard divertor and only 300 °C–500 °C in the SF phase. Peak ELM heat fluxes showed a decreasing trend with decreasing σ, while the plasma stored energy loss due to ELMs ΔW_{MHD} either decreased or remained similar during the transition from the standard divertor to the SF-minus (decreasing σ). The surface temperature rise is given by $\Delta T \sim E_{\text{ELM}}/(A_w \times \tau_{\text{ELM}}{}^{(1/2)})$. Reduced surface heating was expected due to the increased ELM energy deposition time τ_{ELM} and increased A_w as the ELM convective ion heat pulse with energy E_{ELM} travels over an increased field line length $L_{\parallel}$ (assumed being adjacent to the separatrix) connecting the outer midplane to the divertor

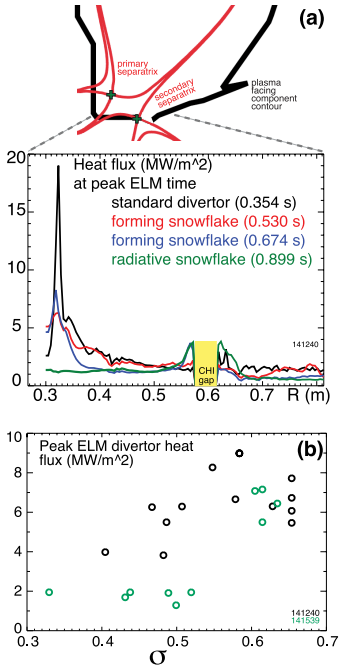

Fig. 6. (a) Peak divertor heat flux at peak ELM times before and during the SF formation, as well as in the radiative SF phase in NSTX. Top inset: two separatrix branches in the asymmetric SF-minus configuration. (b) Peak divertor heat fluxes measured at peak ELM times as the functions of the σ parameter.

target, as also confirmed by modeling [18]. Another possible effect is the theoretically predicted convective mixing of the ELM heat in the null-point region leading to the heat flux partitioning between separatrix branches, and driven by the loss of magneto-hydrodynamic (MHD) equilibrium, ballooning modes and flute-like instabilities in the null region [8]. The emergence of an additional peak in the heat flux (and temperature) profile at the secondary separatrix location (and also where $f\exp$ and L_X were close to those of the standard divertor) and a strong reduction of heat flux at the primary separatrix was consistent with the theoretically predicted SF power sharing effects, and a strong baffling of ELM heat flux in the detached SF-minus. The heat flux in the inner divertor that usually receives more heat during ELMs in tokamaks [19]–[21], was not measured in these experiments.

IV. Snowflake Divertor Experiments in DIII-D

The SF divertor experiments were conducted in DIII-D using a standard highly shaped lower single null H-mode discharge scenario with $B_t = 2$ T, $I_p = 1.2$ MA, $P_{\mathrm{NBI}} \leq 5$ MW, and ion $B \times \nabla B$ drift toward the lower divertor. A divertor cryo-pump was used for particle removal, and D_2 seeding was used for steady-state density control in the range (0.4–0.7) $\times$ n_e/n_G ($\sim$4.5–7.5 $\times$ 10^{19} m^{-3}, where n_G is the Greenwald density [22]).

Inter-ELM peak heat flux reduction in the SF divertor (see standard divertor) was observed in the experiments and attributed mostly to the increased A_{wet} and $L_{\parallel}$. Shown in Fig. 7 are the divertor heat flux profiles measured in 4–5 MW NBI-heated H-modes by infrared thermography under attached divertor conditions [lower n_e $\sim$(4–5.5) $\times$ 10^{19} m^{-3}) with similar low divertor radiated power losses (1.3 MW). Also shown are the parallel heat flux profiles, where the effect of A_{wet} is accounted via the angle between the total magnetic field and the divertor target: $q_{\parallel} = q_{\mathrm{div}}/\sin(\alpha)$, where $\alpha = 0.5 - 2°$. The inter-ELM profiles were conditionally averaged over 20–50 ms during the last 25% of the inter-ELM cycle. In all SF divertor configurations, the innermost SP (SP4 referring to Fig. 7) received the low heat flux of 0.1–0.3 MW/m^2, similar to the standard divertor. Power spreading in the divertor via heat flow into additional divertor legs (SP2 and SP3) was also observed. In the SF-minus, the outer SOL power was split between SP3 and SP1. The fraction of power (and heat flux) deposited in SP3 was typically low, up to 15% of the power measured in the SP1 at $P_{\mathrm{NBI}} \geq 5$ MW, and undetectable at $P_{\mathrm{NBI}} \leq 4$ MW, despite the fact that 30%–60% of the SOL adjacent to the primary separatrix was connected to it. Interestingly, the SP1 received most of the heat flux, which was mitigated due to the increased flux expansion [23]. In the nearly exact SF, most of the outer SOL heat went into the SP1, and a small fraction (again, between 1%–2% and 10%) diffused across the null region into SP2. Heat deposition in the SF-plus was similar, except heat in the additional SPs was rarely detected, likely to be because of the proximity of the 45° divertor tile to the secondary null and the associated high flux expansion. In most cases, A_{wet} accounted for up to 80%–90% of the observed divertor q_{peak} reduction, with the rest attributed to other effects, e.g., spreading to the additional SPs, and not readily quantifiable reduction due to additional diffusive spreading over the increased $L_{\parallel}$ [23], [24].

Radiative SF divertor experiments in DIII-D revealed stronger inter-ELM divertor peak heat flux reduction in comparison with the standard radiative divertor. Radiative divertor conditions in DIII-D are achieved in the standard divertor with carbon and deuterium radiation using D_2 seeding that increases upstream (and core) density [25], [26]. A comparison of the D_2-seeded radiative SF and standard radiative divertor results at $P_{\mathrm{NBI}} = 4 - 5$ MW is shown in Figs. 8 and 9, and can be summarized as follows.

1) Both the radiative SF-plus and SF-minus were compatible with the H-mode confinement albeit with confinement degradation similar to the standard divertor. While the confinement degradation was not associated with the SF formation at lower-to-medium densities, additional D_2 seeding at rates 50–80 torr l/s (to raise the density for radiative divertor onset) resulted in 10%–20% reduction in, e.g., H98$(y, 2)$ and H89L factors and plasma stored energy W_{MHD} in the standard divertor, and up to 30% in H-mode discharges with the radiative (higher density) SF-plus or SF-minus. The degradation was associated with the reduction of pedestal T_e^{ped} and hence pedestal energy [23]. Further H-mode scenario development is necessary to optimize compatibility of the core plasma with radiative SF, as is typically done with the standard radiative divertor [27].
2) Divertor heat flux profiles are compared in Fig. 8(a) and (b). In the standard divertor, the partial detachment led to a significant (up to ten times) peak heat flux reduction (see Fig. 7). In the

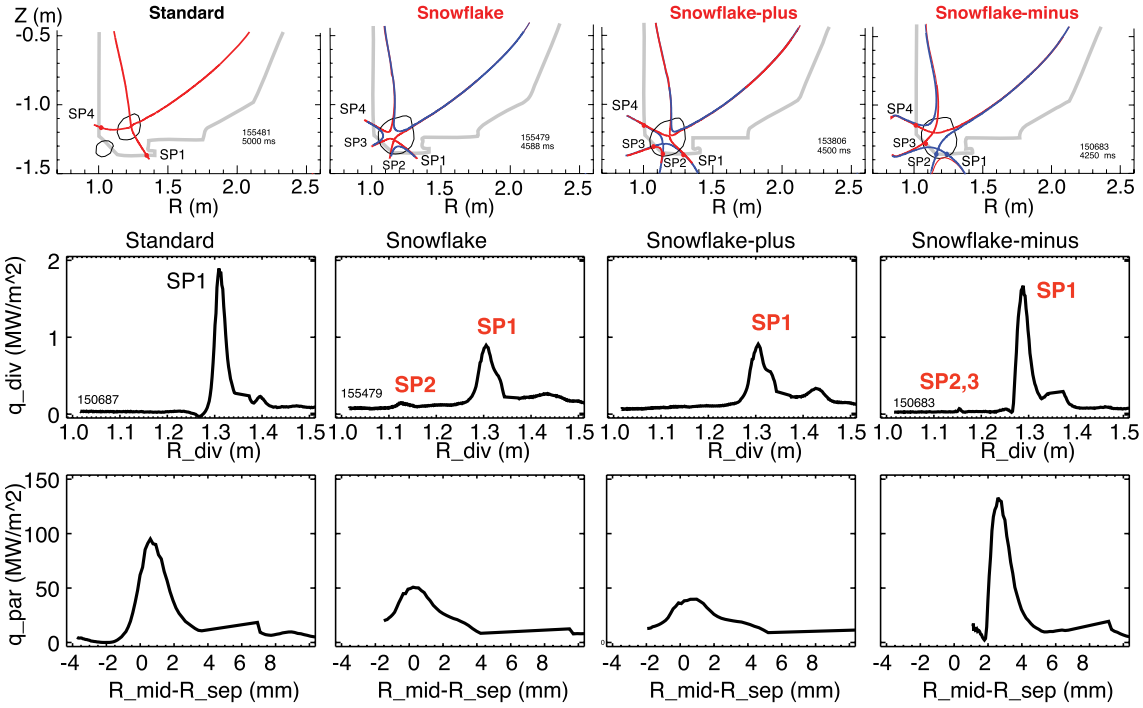

Fig. 7. Experimental equilibria of the standard, SF, SF-plus, and SF-minus divertor configurations in DIII-D. The primary separatrices are shown by the red lines, the secondary by the blue lines. The region $B_p \leq 0.1\ B_{\rm pm}$, where $B_{\rm pm}$ is the outer midplane B_p, is shown by the line surrounding the null(s) region. Inter-ELM divertor deposited and parallel heat flux profiles in the standard ($D \simeq 20$ cm), SF ($D \leq 3$ cm), SF-plus ($D \leq 10$ cm), and SF-minus ($D \leq 11$ cm) configurations.

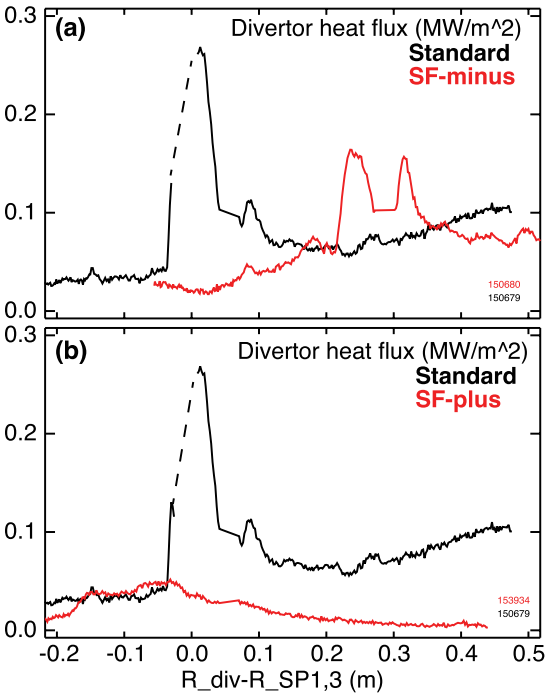

Fig. 8. Inter-ELM divertor heat flux profiles in the standard (a) SF-minus and (b) SF-plus radiative divertors in DIII-D.

radiative SF-minus and SF-plus, a nearly complete power detachment was observed, as heat flux in SP1 was barely detectable. The flux expansion factor could account for most of the difference between the radiative SF-minus and the standard divertor, while in the SF-plus case, the difference was greater.

3) The onset of radiative SF conditions (e.g., increase in impurity radiation and recombination, heat flux reduction) were obtained at core n_e similar (or lower by 10%–20%) to the standard radiative divertor, as shown in Fig. 9(a).

The radiated power was more broadly distributed in the SF configurations, including the additional divertor legs. Shown in Fig. 9(b)–(d) are radiated power distributions in the radiative standard and SF divertors, obtained from tomographic reconstructions of multichannel bolometry data. The lower divertor radiated power was about 2 MW in the radiative standard, SF-plus or minus configurations, differing by 10%–15% (see $P_{\rm SOL}$ ~3–3.5 MW). In the standard divertor, radiation initially peaked in the inner and outer divertor legs, and at the partial detachment onset, the radiative front moved to the X-point [26]. In the SF-minus, radiation also initially peaked in the divertor legs, and, as the SF-minus was formed, it broadly distributed throughout the divertor volume, with occasional peaking at the null points. In the SF-plus, the radiation front was formed in the divertor legs and moved toward the null-point region where it stabilized. The extended connection length region enabled a broader radiation zone.

Initial experiments were also performed to combine the radiative SF divertor configuration with a high-performance advanced tokamak H-mode scenario [28]. The configuration included the upper single null and lower SF-minus with the ion ∇B direction toward the upper divertor, and neon and D_2 seeding. While the peak heat flux reduction was about

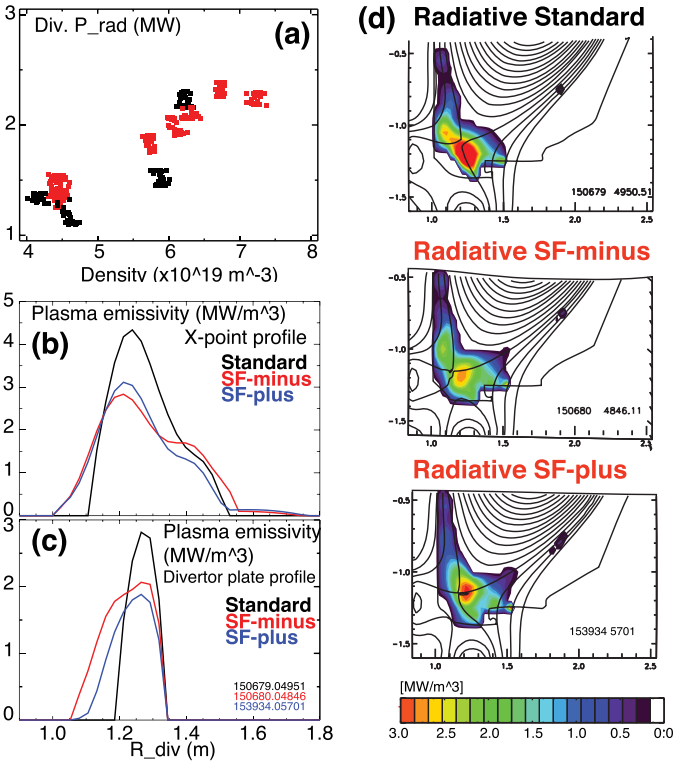

Fig. 9. (a) Divertor radiated power as a function of core plasma density in the standard radiative (black points), and SF-minus and SF-plus configurations (red points). Divertor plasma emissivity radial profiles through (b) X-point and (c) strike point regions. (d) Radiated power distribution from multichordal divertor bolometry.

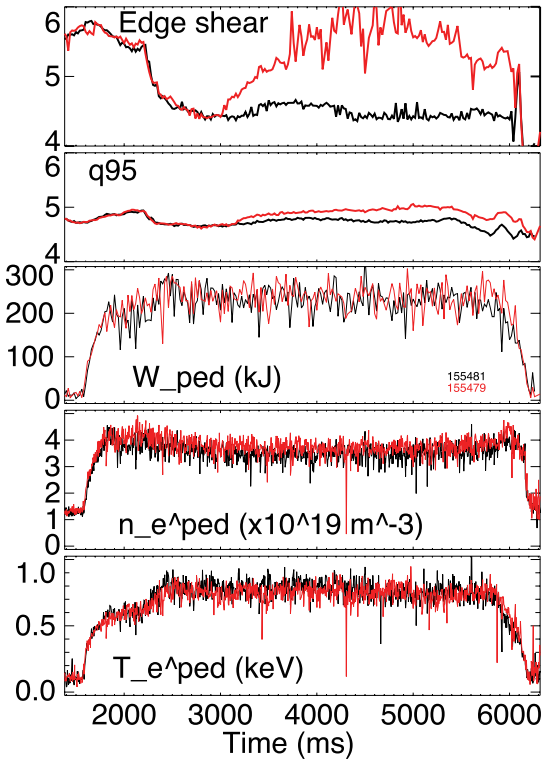

Fig. 10. Edge and pedestal time traces with the standard (black) and SF (red) configurations in DIII-D. (a) Edge magnetic shear. (b) q95. (c) Pedestal energy. (d) Pedestal density. (e) Pedestal temperature.

50% stronger in the radiative SF than in the standard radiative divertor with comparable core confinement (e.g., H98$(y,2)\sim$ 1.30, $\beta_N \sim 2.9$), neon accumulation was 30%–40% higher in the radiative SF case. As the cryopumping was used for neon inventory control, the need for better understanding of compatibility of cryopumping with high flux expansion was concluded.

Returning to the core and pedestal with the SF configuration, we note that core confinement was unaffected at the lower density. The pedestal parameters were modified, as shown in Fig. 10. In the pedestal region, both edge magnetic shear and q_{95} were systematically increased by 10%–30%. Kinetic profiles were weakly affected by the SF configurations. Pedestal top plasma parameters were modestly changed within $\sim$ 15%: with the SF, T_e^{ped} slightly reduced, n_e^{ped} slightly increased, and p_e^{ped} remained nearly constant. Pedestal energy W_{ped} was nearly unaffected at lower n_e. However, some additional degradation of the pedestal T_e was noted in highly radiative SF configurations, leading to the pedestal energy reduction. Changes in the magnetic shear and weak changes in pedestal pressure gradient did not apparently affect the stability of the peeling-ballooning modes, as only small changes in ELM frequency (about 10%–20%) were detected with the SF. The large differences between the SF divertor effect on pedestal ELM stability in NSTX and DIII-D are likely to be due to difference in pedestal operating points in the stability space, i.e., with respect to peeling or ballooning mode stability limits.

The pedestal stored energy lost per ELM ΔW_{ELM} was reduced, as higher q_{95} increased the pedestal collisionality $\nu^*_{\text{ped}} = \pi R q_{95}/\lambda_{e,e}$ and the ELM parallel transit time $\tau_{||}^{\text{ELM}} = 2\pi R q_{95}/c_{s,\text{ped}}$ (the pedestal ion transport time from the mid plane to the target at the sound speed c_s). This was consistent with the Type I ELM scaling of ΔW_{ELM} with ν^*_{ped} found in many tokamaks [29]. In some discharges, the effect was strong, and ΔW_{ELM} was reduced by up to 50% [30], [31]. More typically, however, the reduction was in the range of 5%–20%. At higher density in radiative SF divertor discharges, both ΔW_{ELM} and $\Delta W_{\text{ELM}}/W_{\text{ped}}$ were lower by 10%–20% (see standard divertor) [23].

The SF configuration led to the reduction of ELM energy and ELM peak divertor target temperatures and heat fluxes both at lower n_e and higher n_e (at radiative conditions). As discussed in Section III, the increased $L_{||}$ could lead to reduced target surface temperature rise, and the fast convective transport in the low B_p region driven by instabilities [32] could lead to the ELM heat flux sharing among the additional strike points. These points are consistent with the measurements shown in Fig. 11. Shown are the reduction of ELM energy (fewer ELMs with higher energy) in the SF configuration, and the reduced divertor peak ELM target temperatures measured on the inner and outer targets (see standard divertor). In radiative SF divertor experiments in DIII-D, both the ΔW_{ELM} and the divertor $q_{\text{peak}}^{\text{ELM}}$ were reduced more strongly than in standard radiative divertor, leading to the much reduced peak powers. The peak divertor power was reduced

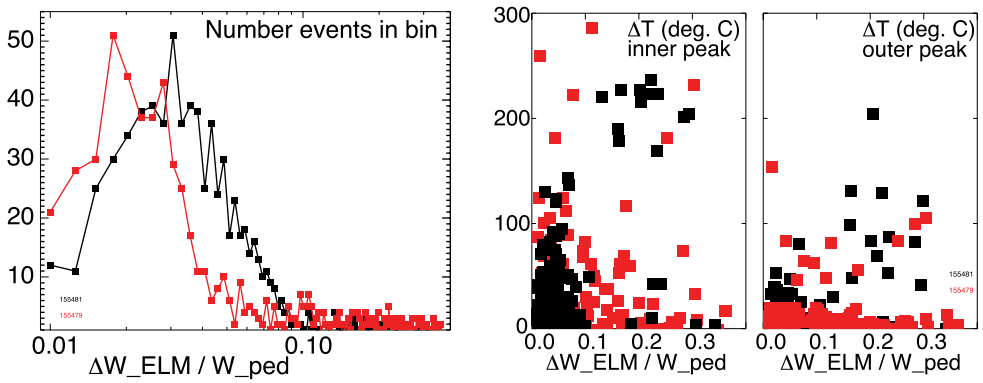

Fig. 11. Distribution of ELM energy normalized to pedestal energy in the standard and SF configurations in DIII-D. Peak divertor temperatures due to ELMs in the inner and outer strike points in the standard and SF configurations.

in the SF-minus by up to 50%–70%, and further reduced in the radiative SF-minus by up to 50%, as compared with the standard divertor [23], suggesting that enhanced radiative dissipation, geometric effects, and power spreading all played a role. The analysis of ELM plasma-wetted areas $A_{\rm wet}^{\rm ELM} = P{\rm div}^{\rm ELM}/q_{\rm peak}^{\rm ELM}$, where $P{\rm div}^{\rm ELM}$ is the divertor power received during an ELM, showed no systematic trends in the outer divertor, and a reduced $A_{\rm wet}^{\rm ELM}$ in the inner divertor in the SF configuration, both at lower n_e and at higher n_e (radiative) conditions.

V. NSTX Upgrade

The NSTX facility has been recently upgraded to new capabilities to enable physics studies to advance the ST as a candidate for fusion nuclear science facility [33]. In NSTX-U, discharges with $I_p \leq 2$ MA and $P_{\rm NBI} \leq 12$ MW and up to 5-s duration are projected to produce steady-state peak divertor heat fluxes in excess of 10 MW/m^2, thereby challenging thermal limits of divertor graphite PFCs [34]. One of the four elements of the NSTX Upgrade research mission is the development of advanced plasma-material interface solutions [33]. The leading heat flux mitigation candidates for NSTX-U are the SF divertor geometry and the impurity-seeded radiative divertor technique, applied to the lower and upper divertors [2].

Research is planned on NSTX-U to test SF magnetic feedback control, and demonstrate steady-state SF configurations with reduced heat flux, compatible with high-β, low collisionality H-mode scenarios [33]. A new set of divertor coils has been installed in NSTX Upgrade, as compared with NSTX. To enable flexibility in divertor configuration and shaping control, an additional divertor coil PF1C has been installed in NSTX-U, as shown in Fig. 12. However, in the initial plasma operations period, three coils will be connected to power supplies: the up–down symmetric PF1A, PF1C, and PF2 coils. A number of magnetic equilibria with SF configurations have been modeled successfully using the predictive free-boundary Grad–Shafranov code ISOLVER. The exact SF, SF-minus, and SF-plus configurations in the lower and upper divertor regions could be realized with the up–down symmetric set of divertor coils operated below their respective current limits, and with plasma currents up to 2 MA.

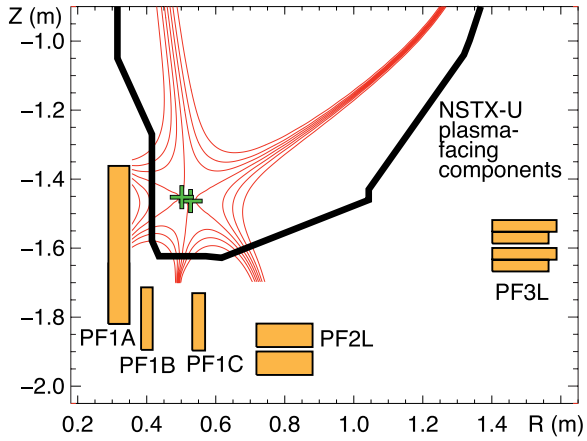

Fig. 12. Upgraded NSTX-U divertor coil set. A modeled SF equilibrium that uses all four divertor coils is shown.

Four divertor coils should enable control of up to four independent parameters, e.g., positions of the null points and strike points. Robust SF configurations were obtained in simulations even when time-varying leakage flux from the time-evolving ohmic solenoid current was included [33]. Shown in Fig. 13 are examples of the standard divertor and SF-plus, SF-minus, and near-exact SF configurations obtained with three divertor coils. All configurations maintained a primary X-point height at about 10 cm above the divertor surface. The divertor coil currents for these configurations and a nominal lower single null configuration are shown in Table II.

The modeled SF equilibria were also used in predictive edge transport modeling with multifluid code UEDGE [35]. Several key modeling results are shown in Fig. 14, while the details are provided in [36]. The model used NSTX-like transport coefficients $\chi_{i,e} = 2 - 4$ m^2/s and $D = 0.5$ m^2/s [37], a neutral model using diffusive treatment in cross-field directions and a full Navier–Stokes treatment in the parallel direction, a fixed fraction (3% carbon) impurity and the ion recycling coefficients $R = 1$ at the wall, and $R = 0.99$ at the divertor plates. The effects of the classical electromagnetic particle drifts were not included. The power flowing into the SOL was equally split between electrons and ions. The model did not include any special transport modifiers in the

TABLE II
COIL CURRENTS FOR MODELED SF EQUILIBRIA SHOWN IN FIG. 13 THAT USE THE COILS AVAILABLE FOR INITIAL EXPERIMENTS IN NSTX-U

Divertor coil	Current limits (kA)	Standard configuration currents (kA)	Near-exact SF configuration currents (kA)	SF-plus configuration currents (kA)	SF-minus configuration currents (kA)
PF1A	19	2.3	3.1	2.8	3.2
PF1B	13	0	0	0	0
PF1C	-8 / + 16	0.4	-1.4	-0.97	-1.3
PF2L	15	1.0	6.6	5.4	6.2

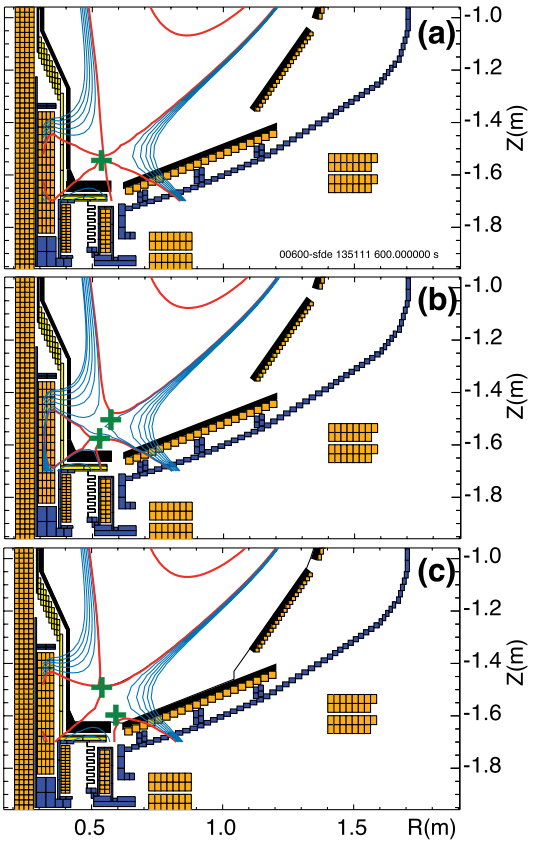

Fig. 13. Modeled SF equilibria using the divertor coil set (PF1A, PF1C, and PF2L as shown in Fig. 12) available in initial NSTX-U experiments. (a) Near-exact SF. (b) SF-plus. (c) SF-minus configurations.

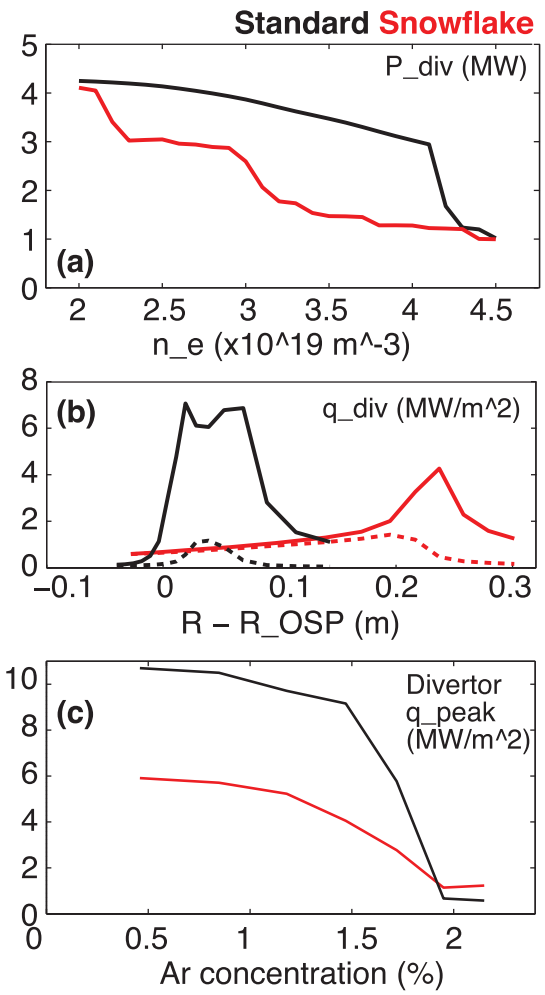

Fig. 14. UEDGE modeling results for NSTX-U standard (black traces) and SF-minus (red traces) divertor configurations. (a) Divertor power as a function of electron density (n_e at the core-boundary interface). (b) Divertor heat flux profiles at $n_e = 3.5 \times 10^{-19}$ m^{-3}—total (including the radiative heating, solid lines) and without the radiative heating flux (dashed lines). (c) Peak divertor heat flux (total, including the radiative heat flux) as a function of argon concentration in a radiative argon-seeded divertor.

null region of the SF configuration; hence, it mostly showed effects of the SF geometry on heat and impurity radiation. The geometric factors were very favorable: in the outer strike point region, $L_{\parallel} \simeq 20-30$ m (see 7–15 m in the standard divertor), and $f\exp \leq 40$ (see 10–20 in the standard divertor). Results for the most challenging $P_{\mathrm{SOL}} = 9$ MW case representative of the 12-MW, 2-MA NBI-heated plasma discharge are shown in Fig. 14. Divertor power as a function of density is shown in Fig. 14(a). A highly radiative scenario occurs in the SF configuration at a much lower density, enabling a greater power loss (with respect to the standard divertor), and a larger operating window with reduced $q$div at lower n_e. Total divertor heat fluxes (that include radiative heating) and the heat fluxes without radiative heating at $n_e = 3.5 \times 10^{-19}$ m^{-3} are shown in Fig. 14(b). In the outer divertor, high $q_{\mathrm{peak}} \simeq 7$ MW/m^2 was obtained with the standard divertor, and only 3–4 MW/m^2 in the SF-minus configuration. The figures suggest that both the flux expansion and the additional radiated power loss are the leading q_{peak} reduction mechanisms in the SF-minus model. The inner divertor region was found to be highly radiative (possibly with a detached strike point) in both configurations. Impurity-seeded divertors (with neon and argon) were also analyzed. Fig. 14(c) shows that 50% less argon is needed in

the SF-minus configuration to achieve similar q_{peak} reduction factors (see standard divertor). The UEDGE modeling results support the SF divertor as a leading steady-state divertor power exhaust solution for NSTX-U.

VI. Discussion and Conclusion

The emerging understanding of inter-ELM and ELM divertor heat transport and radiation in the SF divertor from NSTX and DIII-D experiments provides support to the SF divertor configuration as a promising power exhaust concept. In this section, we discuss outstanding physics issues that need to be resolved in existing and future tokamaks in order to design a tokamak-based reactor plasma-material interface based on the SF divertor concept.

The SF configuration has been realized on the NSTX and DIII-D tokamaks without any changes to existing poloidal field coil sets. Equilibria designs were performed using free boundary Grad–Shafranov equilibrium codes. A variety of SF divertor equilibria have been modeled for NSTX Upgrade, with both a full coil sets and a reduced coil sets available in initial years. An SF configuration control algorithm based on the real-time null tracking [12] is being implemented in the plasma control system.

The SF experiments have shown no detrimental effects on core confinement. The pedestal structure and ELM properties (energy and frequency) have been affected differently in NSTX and DIII-D, suggesting that MHD stability was modified by the presence of the second null. However, the SF effects on the ELM regimes and stability depend on the pedestal stability operating point. A systematic analysis of all possible causes is required, since the effects of higher edge magnetic shear and modified plasma pressure gradient due to the SF could be mixed with the effects of both plasma shaping and edge parameter variations. Increased prompt ion loss through the second-order null region was predicted theoretically [38] and may affect the edge electric field and velocity shear, and however, no measurements have been performed to verify this.

The increased magnetic flux expansion in the vicinity of the main strike points, the increased connection length in the SOL, and the increased specific divertor volume has been demonstrated. The geometry modifications led to significantly lower deposited divertor heat fluxes. The exact attribution of this reduction to particular geometry effects was not possible. In both experiments, the strike points were generally located in the SF-induced low B_p zone; hence, the flux expansion lowered heat flux in the strike points, sometime to very low levels beyond experimental detection limit. Future SF experiments can focus on divertor heat and particle (impurity) transport studies as the functions of geometry properties and plasma collisionality (e.g., in a transition from low recycling to high recycling and detached), utilizing the SF divertor as a laboratory for divertor physics. Predicted effects include increased radial transport and temperature drop in each divertor leg, a longer divertor particle residence time, disconnection of turbulence along the flux tube due to stronger shearing in the SF region, and increased flux tube volume and radiation. Some of these effects have been observed and characterized through modeling [18], [37], [39].

The attractive SF divertor property of particle and heat flux sharing between additional strike points between and during ELMs was observed experimentally [24]. However, the associated transport mechanism is not well understood and can include particle drifts [40], flute-like and ballooning instabilities that can lead to fast convection [7], [8], [32], [41], [42], and magnetic field stochastization. Identification and development of a multidevice scaling of the heat flux sharing effect are desirable.

Radiative SF experiments used D_2 seeding and intrinsic carbon impurities, or additional impurity seeding (CD_4 in NSTX, neon in DIII-D), and demonstrated additional peak heat flux reduction, including peak ELM heat fluxes (“ELM buffering”), nearly full power detachment, and increased divertor radiation (see standard radiative divertor) [11], [23], [28], [43]. Again, the results in NSTX and DIII-D differed consistently with the standard radiative divertor results differing in the two devices. In NSTX, radiative SF divertor was naturally obtained, and no core confinement degradation was observed. In DIII-D, additional gas seeding was required to induce a radiative SF divertor, and a modest degradation in core confinement was observed. The present studies have not yet addressed radiative SF divertor with high divertor radiated power fractions, e.g., $f_{\text{rad}} \geq 0.6 \times P_{\text{SOL}}$. The SF impurity radiation distribution, dynamics of radiative condensation instability formation and threshold, impurity screening, and compatibility with particle control techniques (e.g., cryopump), and combining the SF divertor with applied 3-D magnetic fields for MHD and ELM control are all outstanding issues and could provide critical information for reactor applications.

In conclusion, recent NSTX and DIII-D experiments have confirmed many predicted SF divertor properties, supporting it as an attractive candidate concept for divertor power exhaust in the future devices. In the near term, experiments are planned in NSTX Upgrade to clarify the transport and radiative properties in the SF configuration.

Acknowledgment

The authors would like to thank the NSTX and the DIII-D Teams for plasma, NBI, and diagnostic operations.

References

[1] V. A. Soukhanovskii, “Advanced divertor magnetic configurations for tokamaks: Concepts, status, future,” in *Proc. Edge Coordinating Committee Fall Tech. Meeting*, Nov. 2014, pp. 1–35. [Online]. Available: http://fire.pppl.gov/APS-DPP14_Divertor_Soukhanovskii.pdf

[2] D. D. Ryutov, “Geometrical properties of a ‘snowflake’ divertor,” *Phys. Plasmas*, vol. 14, no. 6, p. 064502, 2007.

[3] F. Piras *et al.*, “‘Snowflake’ H mode in a tokamak plasma,” *Phys. Rev. Lett.*, vol. 105, no. 15, p. 155003, 2010.

[4] V. A. Soukhanovskii *et al.*, “Taming the plasma–material interface with the ‘snowflake’ divertor in NSTX,” *Nucl. Fusion*, vol. 51, no. 1, p. 012001, 2011.

[5] S. Allen *et al.*, “PD/1-2: Initial snowflake divertor physics studies on DIII-D,” in *Proc. 24th IAEA FEC-IAEA CN-197*, San Diego, CA, USA, Oct. 2012, paper PD/1-2.

[6] G. Calabrò *et al.*, “EAST snowflake experiment: Scenario development and edge simulations,” in *Proc. 25th IAEA FEC-IAEA CN-221*, Saint Petersburg, Russia, Oct. 2014, paper Ex/P3-4.

[7] D. D. Ryutov, R. H. Cohen, T. D. Rognlien, and M. V. Umansky, “A snowflake divertor: A possible solution to the power exhaust problem for tokamaks,” *Plasma Phys. Control. Fusion*, vol. 54, no. 12, p. 124050, 2012.

[8] D. D. Ryutov *et al.*, "Theory and simulations of ELM control with a snowflake divertor," in *Proc. 24th IAEA FEC-IAEA CN-197*, San Diego, CA, USA, Oct. 2012, paper TH/P4-18.
[9] D. D. Ryutov, R. H. Cohen, T. D. Rognlien, and M. V. Umansky, "The magnetic field structure of a snowflake divertor," *Phys. Plasmas*, vol. 15, no. 9, p. 092501, 2008.
[10] D. D. Ryutov, M. A. Makowski, and M. V. Umansky, "Local properties of the magnetic field in a snowflake divertor," *Plasma Phys. Control. Fusion*, vol. 52, no. 10, p. 105001, 2010.
[11] V. A. Soukhanovskii *et al.*, "Snowflake divertor configuration studies in National Spherical Torus Experiment," *Phys. Plasmas*, vol. 19, no. 8, p. 082504, 2012.
[12] E. Kolemen *et al.*, "Heat flux management via advanced magnetic divertor configurations and divertor detachment," *J. Nucl. Mater.*, vol. 463, pp. 1186–1190, Aug. 2015.
[13] D. K. Mansfield *et al.*, "Transition to ELM-free improved H-mode by lithium deposition on NSTX graphite divertor surfaces," *J. Nucl. Mater.*, vols. 390–391, pp. 764–767, Jun. 2009.
[14] R. Maingi *et al.*, "Edge-localized-mode suppression through density-profile modification with lithium-wall coatings in the National Spherical Torus Experiment," *Phys. Rev. Lett.*, vol. 103, p. 075001, Aug. 2009.
[15] V. A. Soukhanovskii *et al.*, "Divertor heat flux mitigation in high-performance H-mode discharges in the National Spherical Torus Experiment," *Nucl. Fusion*, vol. 49, no. 9, p. 095025, 2009.
[16] V. A. Soukhanovskii *et al.*, "Divertor heat flux mitigation in the National Spherical Torus Experiment," *Phys. Plasmas*, vol. 16, no. 2, p. 022501, 2009.
[17] V. A. Soukhanovskii *et al.*, "Divertor heat flux mitigation with impurity-seeded standard and snowflake divertors in NSTX," in *Proc. 39th EPS conf. 16th Int. Congr. Plasma Phys.*, Stockholm, Sweden, 671 2012, paper P5.049.
[18] T. D. Rognlien, R. H. Cohen, D. D. Ryutov, and M. V. Umansky, "Comparison of ELM heat loads in snowflake and standard divertors," *J. Nucl. Mater.*, vol. 438, pp. S418–S421, 2013.
[19] ITER Physics Expert Group on Divertor, ITER Physics Expert Group on Divertor Modelling and Database, and ITER Physics Basis Editors, "Chapter 4: Power and particle control," *Nucl. Fusion*, vol. 39, no. 12, p. 2391, 1999.
[20] A. Loarte *et al.*, "Chapter 4: Power and particle control," *Nucl. Fusion*, vol. 47, no. 6, p. S203, 2007.
[21] B. Lipschultz *et al.*, "Plasma–surface interaction, scrape-off layer and divertor physics: Implications for ITER," *Nucl. Fusion*, vol. 47, no. 9, p. 1189, 2007.
[22] M. Greenwald *et al.*, "A new look at density limits in tokamaks," *Nucl. Fusion*, vol. 28, no. 12, p. 2199, 1998.
[23] V. A. Soukhanovskii *et al.*, "Radiative snowflake divertor studies in DIII-D," *J. Nucl. Mater.*, vol. 463, pp. 1191–1195, Aug. 2015.
[24] V. A. Soukhanovskii *et al.*, "Developing physics basis for the radiative snowflake divertor at DIII-D," in *Proc. 25th IAEA FEC-IAEA CN-221*, Saint Petersburg, Russia, Oct. 2014, pp. 1–15, paper EX/7-4.
[25] T. W. Petrie *et al.*, "Radiative divertor experiments in DIII-D with D_2 injection," *Nucl. Fusion*, vol. 37, no. 3, p. 321, 1997.
[26] M. E. Fenstermacher *et al.*, "Physics of the detached radiative divertor regime in DIII-D," *Plasma Phys. Control. Fusion*, vol. 41, no. 3A, pp. A345–A355, 1999.
[27] T. W. Petrie *et al.*, "Compatibility of the radiating divertor with high performance plasmas in DIII-D," *J. Nucl. Mater.*, vols. 363–365, pp. 416–420, Jun. 2007.
[28] T. W. Petrie *et al.*, "Application of the radiating divertor approach to innovative tokamak divertor concepts," *J. Nucl. Mater.*, vol. 463, pp. 1225–1228, Aug. 2014.
[29] A. Loarte *et al.*, "ELM energy and particle losses and their extrapolation to burning plasma experiments," *J. Nucl. Mater.*, vols. 313–316, pp. 962–966, Mar. 2003.
[30] D. Hill and The DIII-D Team, "DIII-D research towards resolving key issues for ITER and steady-state tokamaks," *Nucl. Fusion*, vol. 53, no. 10, p. 104001, 2013.
[31] H. Yamada, "Magnetic confinement experiments: Plasma–material interactions, divertors, limiters, scrape-off layer (EX/D), stability (EX/S), wave–plasma interactions, current drive, heating, energetic particles (EX/W)," *Nucl. Fusion*, vol. 53, no. 10, p. 104025, 2013.
[32] D. D. Ryutov, R. H. Cohen, T. D. Rognlien, and M. V. Umansky, "Plasma convection near the magnetic null of a snowflake divertor during an ELM event," *Contrib. Plasma Phys.*, vol. 52, pp. 539–543, Jun. 2012.
[33] J. E. Menard *et al.*, "Overview of the physics and engineering design of NSTX upgrade," *Nucl. Fusion*, vol. 52, no. 8, p. 083015, 2012.
[34] T. K. Gray, R. Maingi, V. A. Soukhanovskii, J. E. Surany, J.-W. Ahn, and A. G. McLean, "Dependence of divertor heat flux widths on heating power, flux expansion, and plasma current in the NSTX," *J. Nucl. Mater.*, vol. 415, no. 1, pp. S360–S364, 2011.
[35] T. D. Rognlien, J. L. Milovich, M. E. Rensink, and G. D. Porter, "A fully implicit, time dependent 2-D fluid code for modeling tokamak edge plasmas," *J. Nucl. Mater.*, vols. 196–198, pp. 347–351, Dec. 1992.
[36] E. T. Meier, S. Gerhardt, J. E. Menard, T. D. Rognlien, and V. A. Soukhanovskii, "Modeling divertor concepts for spherical tokamaks NSTX-U and ST-FNSF," *Nucl. Fusion*, vol. 55, no. 8, p. 086002, 2015.
[37] E. T. Meier *et al.*, "Modeling detachment physics in the NSTX snowflake divertor," *J. Nucl. Mater.*, vol. 463, pp. 1200–1204, Aug. 2015.
[38] D. D. Ryutov and M. V. Umansky, "Ion drifts in a snowflake divertor," *Phys. Plasmas*, vol. 17, no. 1, p. 014501, 2010.
[39] T. Lunt *et al.*, "First EMC3-Eirene simulations of the TCV snowflake divertor," *Plasma Phys. Control. Fusion*, vol. 56, no. 3, p. 035009, 2014.
[40] G. P. Canal, "Sawtooth generated magnetic islands and the properties of the snowflake divertor," Ph.D. dissertation, École Polytechn. Fédérale Lausanne, Lausanne, Switzerland, 2014.
[41] W. A. Farmer and D. D. Ryutov, "Axisymmetric curvature-driven instability in a model divertor geometry," *Phys. Plasmas*, vol. 20, no. 9, p. 092117, 2013.
[42] D. D. Ryutov, R. H. Cohen, W. A. Farmer, T. D. Rognlien, and M. V. Umansky, "The 'churning mode' of plasma convection in the tokamak divertor region," *Phys. Scripta*, vol. 89, no. 8, p. 088002, 2014.
[43] V. A. Soukhanovskii *et al.*, "Divertor heat flux mitigation with impurity-seeded standard and snowflake divertors in NSTX," in *Proc. 39th EPS Conf. Plasma Phys., EPS 16th Int. Congr. Plasma Phys.*, vol. 3. 2012, pp. 1682–1685.

Authors' photographs and biographies not available at the time of publication.